Autonomous landing of underwater vehicles using high resolution bathymetry

Mehul Sangekar, *Member, IEEE,* Blair Thornton, *Member, IEEE,* Adrian Bodenmann, and Tamaki Ura, *Life Fellow, IEEE*

Abstract

The ability to land on the seafloor expands the envelope of tasks that underwater vehicles can carry out during survey and inspection. However, even though remotely operated vehicles routinely land during their operations, autonomous underwater vehicles (AUVs) lack the sensing and data processing capabilities needed to identify safe, stable landing sites. Here, an algorithm is developed that uses mm-resolution bathymetry to detect regions where an AUV of known geometry can safely and stably land on the seafloor. The algorithm uses physical models that consider vehicle geometry, seafloor slope, roughness, friction and currents. It can identify the most suitable of multiple candidate sites based on a landing cost function. The performance of the algorithm is evaluated using seafloor bathymetry data that was obtained using an AUV equipped with a high resolution laser mapping system on the slopes of the Takuyo Daigo seamount in the Northwest Pacific. The algorithm successfully identified multiple landing sites along a 500 m transect on the slopes of the surveyed seamount. The study demonstrates that safe, reliable AUV landing operation is feasible in actual seafloor environments.

M. Sangekar is a project researcher with the Institute of Industrial Science, The University of Tokyo (e-mail: mehul@iis.u-tokyo.ac.jp)

B. Thornton is an Associate Professor at the Maritime Robotics Laboratory, Southampton Marine and Maritime Institute, Faculty of Engineering and Physical Science, The University of Southampton, with an adjunct position at the Institute of Industrial Science, The University of Tokyo (e-mail: b.thornton@soton.ac.uk)

A. Bodenmann is a senior research assistant at the Maritime Robotics Laboratory, Southampton Marine and Maritime Institute, University of Southampton, Southampton, UK (e-mail: adrian.bodenmann@soton.ac.uk)

T. Ura is a Distinguished Professor at the Center for Socio-Robotic Synthesis, Kyushu Institute of Technology (e-mail: ura@lsse.kyutech.ac.jp)

This work was supported by the Japanese Ministry of Education under the Program for the ”Development of Fundamental Tools for the Utilization of Marine Resources”.

Index Terms

Autonomous landing, Seafloor observations, Seafloor mapping, Structured light, Autonomous Underwater Vehicle

I. INTRODUCTION

The use of unmanned underwater vehicles for exploration of mineral deposits [1], such as manganese crusts [2], manganese nodules [3] and seafloor massive sulfides [4] has gained momentum in recent years. While high resolution bathymetric maps of the seafloor generated using acoustic [5] or visual [6] mapping systems are useful for recognizing visible and morphological seafloor features [7], [8], measurement of chemical composition [9] or frictional coefficient [10] of seafloor deposits require direct contact for obtaining measurements. There have been significant developments over the past decade that provide in-situ methods to make measurements of the chemical and geological properties of the seafloor, such as underwater microscopy [11], gamma radiation measurements [12], [13], laser induced breakdown spectroscopy (LIBS) [14], laser Raman spectroscopy [15], [16] and seafloor stiffness and frictional coefficients [17]. The development of these new classes of analytical sensors that requires direct contact motivates the development of landing capabilities for Autonomous Underwater Vehicles (AUVs) to deliver these capabilities in a more scalable manner. The underwater terrain however, can change abruptly on spatial scales that cannot be observed from the surface. Therefore the reliable use of in-situ instruments such as those described, and the safety of the underwater vehicle requires real-time detection of suitable landing sites. Although remotely operated vehicle (ROV) pilots routinely identify safe landing sites and perform manipulations or in-situ chemical measurements with the instruments described, AUVs currently lack the sensing and data processing capabilities needed for these tasks.

In this research, we developed a framework to enable an underwater vehicle to autonomously identify safe landing sites based on in-situ measurements. The design concept of an underwater vehicle is proposed, identifying the hardware modifications needed for landing of AUVs on the seafloor. This includes a landing skid, and a mm-resolution laser mapping system used to detect safe landing areas. The conditions for safe landing are identified and used to develop an algorithm that uses the mm-resolution bathymetry information to identify landing areas considering the geometry and righting moment of the AUV. The algorithm detects safe landing sites along different headings, selecting the most suitable landing site based on a cost function that takes

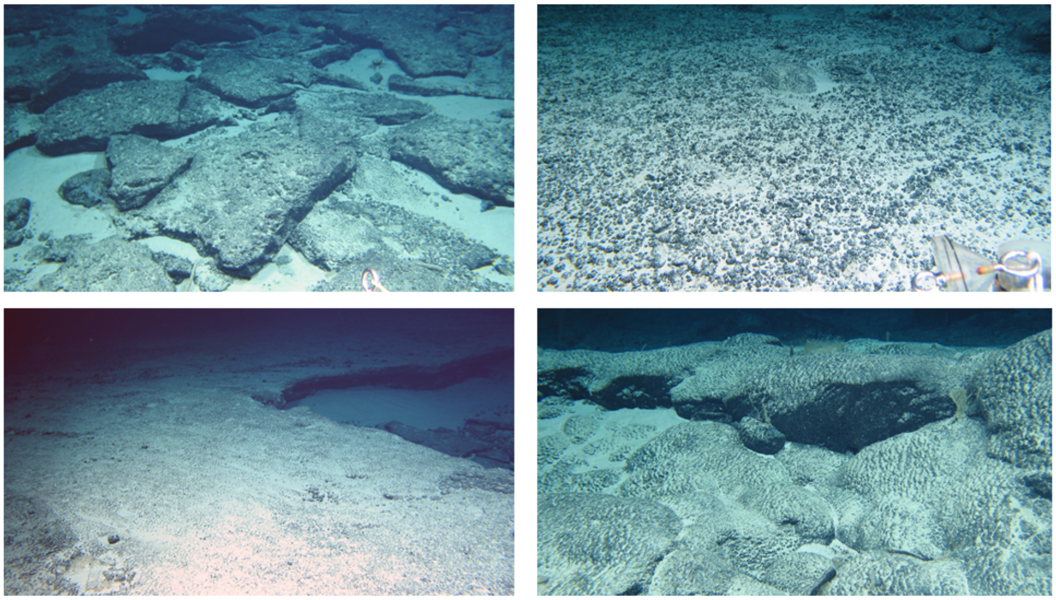

Fig. 1. Different seafloor terrain at Takuyo Daigo seamount [18]. Clockwise, from top left: Broken slabs in sand, nodules, pillowy crusts and continuous flat crusts

into account the slope and rugosity of the seafloor. The performance of the algorithm is verified by analysing more than 750 m^2 of mm-resolution seafloor bathymetry obtained by an AUV along a 500 m transect on the slopes of the Takuyo Daigo seamount (located in the Northwest-Pacific) at an average depth of 1400 m. The results demonstrate the feasibility of safe autonomous landing in real seafloor terrains.

The complexity of seafloor topology (see Fig. 1) prohibits vehicles from simply landing at random locations and requires the identification and intelligent choice of landing sites. At the same time, the spatial scales relevant to AUV landing are too small to be observed by ship-board acoustic multibeam. Therefore, in order for an AUV to identify landing sites during its survey, it should be equipped with a mapping system capable of generating bathymetry with sufficiently high resolution, e.g. using light sectioning [19], [20], [21]. Even though landing site detection for aerial vehicles has been studied in [22], [23], the conditions essential for safe landing in underwater environments has not been sufficiently investigated. Simulations for control, navigation and dynamics of AUVs with landing capabilities have been reported in [24], [25]. However, these previous works do not develop the sensing and data processing methods needed to automatically identify areas where a vehicle can land safely. Regarding methods to analyse seafloor terrains, Fourier analysis based segmentation and 3D alignment was described in

[26], [27]. Other methods for surface classification using wavelets [28] have also been described, but have not been applied to landing site identification. Early works by our group demonstrated a landing algorithm using Fourier analysis to separate flat ground surface from objects on the seafloor [29]. The algorithm rejected all protruding objects as non-landable areas, and only considered flat regions for landing. This work builds on our previous studies, identifying the geometric conditions where it is possible to land on protruding objects and to land on slopes, considering the righting moment of the vehicle

The remainder of this paper is organized as follows; Section II describes the hardware requirements for landing, including the conceptual design of an underwater vehicle capable of landing and its high resolution mapping system for generating bathymetry with mm-resolution. In Section III, the different steps of the algorithm to identify landing sites are described and demonstrated by simulating its performance on seafloor data obtained using an equivalent high resolution mapping system. Section IV applies the algorithm to more than 750 m^2 of seafloor bathymetry obtained using an AUV during an underwater survey. Section V presents the conclusions of this work.

II. LANDING HARDWARE REQUIREMENTS

A. Vehicle hardware

The hardware requirements for vehicles to perform landing operations are sufficiently different to standard vehicles to warrant specific consideration. In this work, we propose a vehicle concept with negative buoyancy during operation. This minimises the use of vertical thrusters during landing operations, allowing the vehicle to remain stationary and vibration free whilst landed and saves power. The negative buoyancy also means that the vehicle can land passively, without the use of its thrusters during its final stage of descent in order to minimize agitation of loose sediments.

The features of the vehicle can be seen in the Fig. 2. Independent heave, surge, sway and heading control are needed to allow the vehicle to operate at low speeds manoeuvres and hover when necessary. Two horizontal thrusters provide surge and heading control. Two thrusters oriented away from the centre of the vehicle and inclined at 22.5° with the vertical, control sway and heave. The inclined thrusters direct thrust away from the area directly below the vehicle to minimizing the disturbance of sand and sediments during landing. A nylon landing skid distributes the vehicle's weight and provides a stable footing when the vehicle has landed. This also provides enough clearance to protect the sensors on the the vehicle.

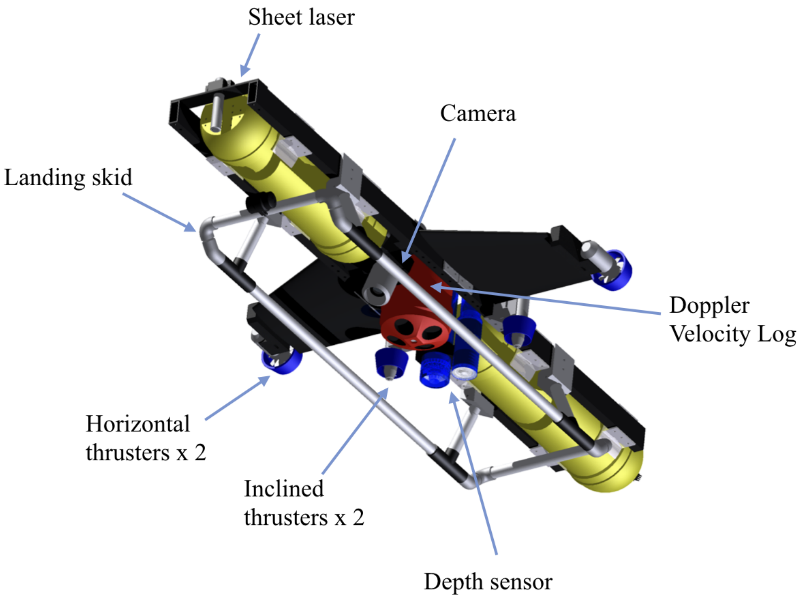

Fig. 2. Concept design of a landing vehicle

The vehicle is designed to be negatively buoyant to allow for landing. Although variable buoyancy engines are available [30], these typically have a capacity of 1 L, and the limited change in buoyancy imposes limits on the conditions under which a vehicle can remain securely landed. Here, a hydrodynamic solution is chosen using a fixed wing NACA651412 profile to offset the negative buoyancy during forward motion as this approach can compensate for a large change in buoyancy. This profile produces lift at zero angle of attack and so minimising the vehicle's drag. During slow manouvres the vehicle is still able to hover, and methods such as the two drop weight method can be used for diving and fail-safe surfacing [31]. The vehicle has a standard navigation suite, consisting of a 1.2 MHz Doppler Velocity Log (DVL), raised more than 30 cm of the bottom of the vehicle to provide bottom lock even when landed, a compass based Attitude Heading Reference System (AHRS), and pressure depth sensor. In addition to standard localisation, the pressure sensor and DVL range can also be used to measure vertical motion during landing and confirm the vehicle remains stationary on the seafloor once landed.

For short distances of travel, the relative motion of an underwater vehicle can be estimated through dead reckoning with an error accumulation of 2 to 5% of the distance travelled for relatively modestly priced solutions, and 0.1% for high-end systems. These would provide a relative position error of 0.5 m to 1.25 m, and 2.5 cm when revisiting a specific location within a 25 m long map segment considered in this work for landing site analysis, where further increases in accuracy can be achieved by implementing SLAM or terrain aided navigation methods. While accurate positioning is an essential, fundamental aspect of AUV behaviour, the solutions required here are not specific to landing operations and further details on the various approaches can be found in [32].

B. High resolution mapping system

A high resolution mapping system using light sectioning is used to generating millimeter resolution bathymetry, as illustrated in Fig. 3 [21]. The system comprises of a sheet laser projecting a line on the seafloor from a mapping altitude a and a camera offset by a distance b from the laser with vertical mounting angle ϕ_m. The sheet laser projects a line on the seafloor whose projection is captured by the camera with horizontal and vertical opening angles ϕ_h and ϕ_v respectively. By detecting the laser line in the image captured by the camera, it is possible to determine the relative coordinates of each recognised point in the laser line. These can then be used to generate continuous bathymetry measurements in the earth-fixed coordinate system based on the pose of the vehicle.

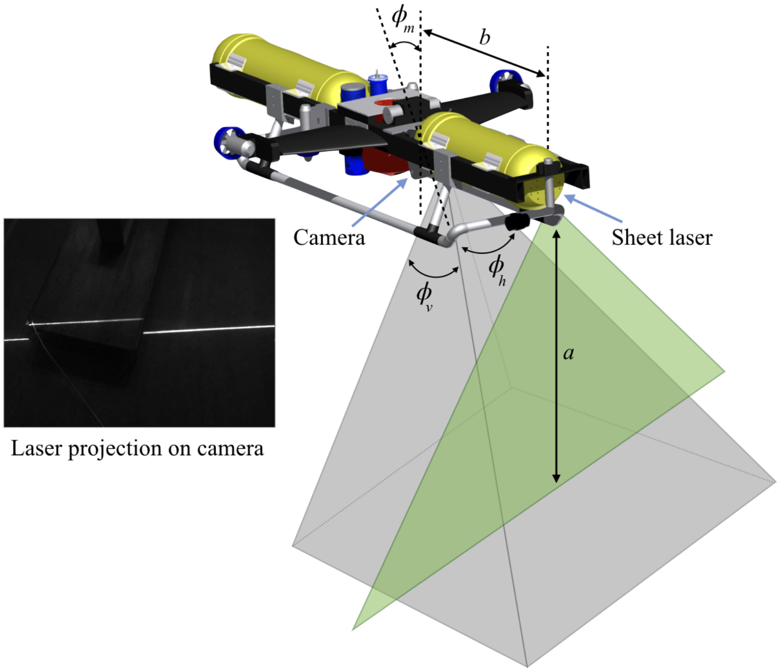

Fig. 3. Setup and mechanism of the high resolution mapping system

III. AUTONOMOUS LANDING ALGORITHM

This section describes the conditions that need to be satisfied in order to achieve safe landing. These are illustrated using high resolution bathymetric data collected by the vehicle BOSS-A at the Takuyo Daigo seamount during the KR16-01 cruise of R/V Kairei [18], [20]. The specifications of the laser mapping system used to collect the data are given in Table I. These landing conditions are used to develop an autonomous landing algorithm that consists of the following steps:

- *Surface mapping:* Convert high resolution point clouds generated by the mapping system into a bathymetry surface with uniform lateral resolution.
- *Landing area detection:* Identify landing areas within sections of bathymetry that satisfy the criteria for safe landing developed in this work.
- *Site identification:* Within the detected landing areas, identify candidate landing sites that are large enough for a vehicle of defined geometry to fit along a certain heading.
- *Site selection:* Landing site properties are extracted for all the candidate sites and a cost function is defined to assess their suitability. The site with minimum landing cost is selected as the final landing site.

TABLE I

PROPERTIES OF THE MAPPING SYSTEM

Property	**Value**
Mapping altitude a	2 m
Baseline between camera and laser b	1.03 m
Vertical mounting angle of camera ϕ_m	20°
Horizontal opening angle of camera ϕ_h	60.2°
Vertical opening angle of camera ϕ_v	50.4°
Along-track resolution	4 mm
Cross-track resolution	3 mm
Vertical resolution	6 mm

A. Surface mapping

Fig. 4a shows a 25 m section of laser bathymetry mapped at a heading of 230° using the method described by Bodenmann et al., [21]. Each point in the point cloud has a known position in the north, east and depth directions. The unstructured points are resampled to a uniform lateral grid resolution of $g_{res} = 10\,\mathrm{mm}$, as shown in (see Fig. 4b). This resolution is chosen as it is sufficiently high to resolve any surface protrusions that may affect landing.

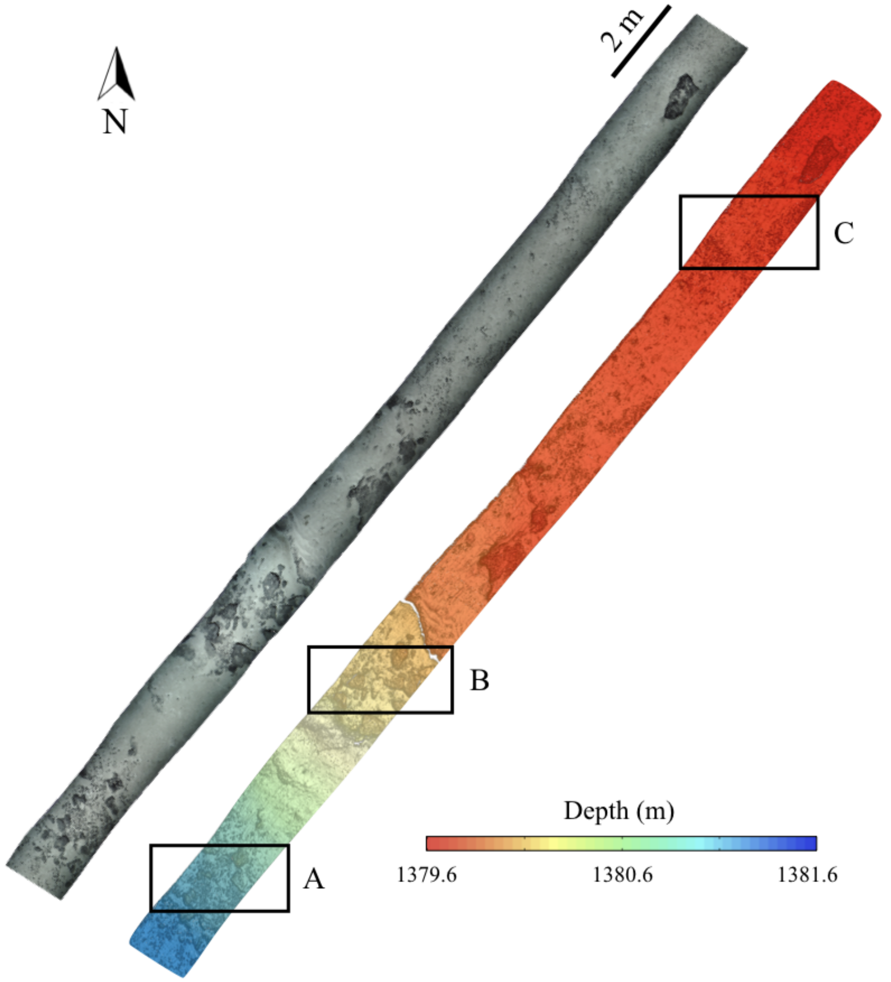

(a) Top view orthographic projection of a 3D seafloor color reconstruction (left) and its corresponding hill shaded depth map (right).

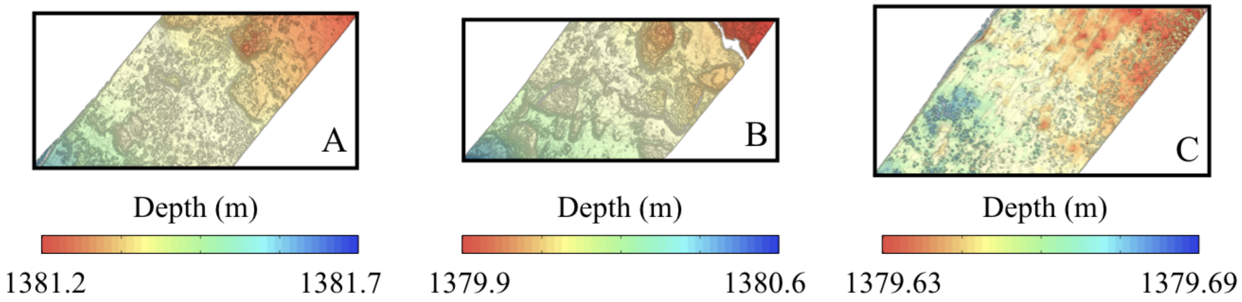

(b) Detailed views of bathymetric data resampled to a uniform lateral grid resolution of $g_{res} = 10\,\mathrm{mm}$, corresponding to the three areas A,B and C in Fig. 4a.

Fig. 4. Seafloor bathymetry mapped using the high resolution laser mapping system mounted on a vehicle

B. Landing area detection

1) Identifying landing conditions: In order to detect safe landing areas, a number of physical conditions need to be locally satisfied in the bathymetry. The effects of slope on landing are analyzed considering the vehicle's righting moment, seafloor friction and currents. The effects of protrusions on landing are analyzed considering their height. The vehicle parameters needed to judge safe landing are illustrated in Fig. 5, with specific values used in this study shown in Table II.

TABLE II

PHYSICAL PROPERTIES OF UNDERWATER VEHICLE

Property	**Description**	**Value**
l_u	length of landing vehicle	1.7 m
b_u	width of landing vehicle	0.5 m
h_u	height of landing vehicle	0.40 m
F_G	force of gravity	637 N (mass 65 Kg)
F_B	force of buoyancy	608 N (mass 62 Kg)
F_R	net downward force	29 N
d_g	vertical distance to C_G	0.25 m
d_m	vertical distance between C_G and C_B	0.05 m

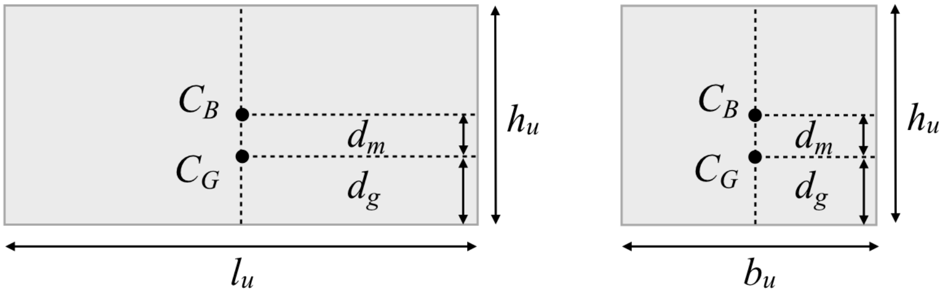

Fig. 5. Side and front view of a vehicle with parameters used to determine landing conditions

Sloping surfaces: The criteria for landing success is considered as when the vehicle can remain stationary and in full contact with the seafloor. Here, we determine the minimum slope on which a vehicle of known geometry and righting moment can meet this condition. The analysis is performed along different orientations of the vehicle with respect to the slope ψ, to find the maximum slope θ_c where successful landing is possible (see Fig. 6).

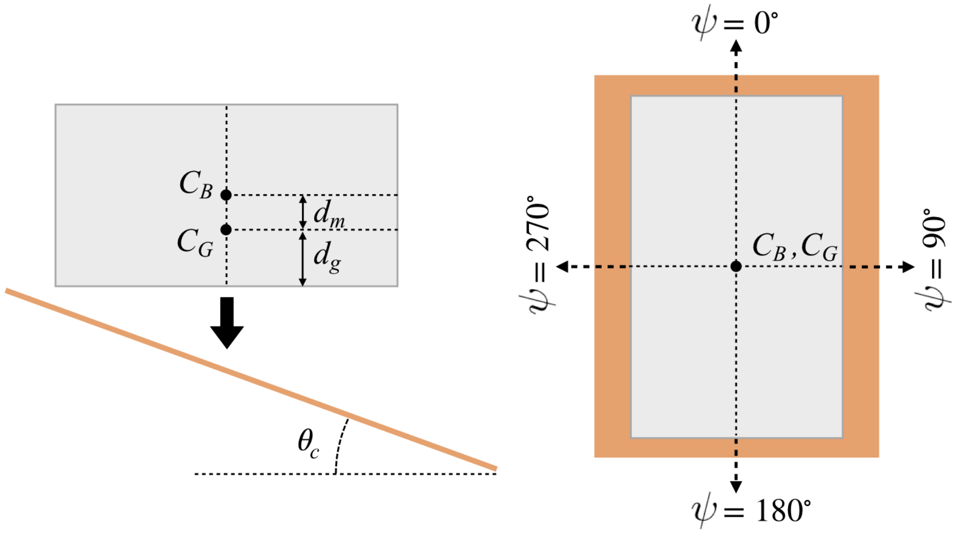

Fig. 6. Side and top view of a vehicle landing on a slope

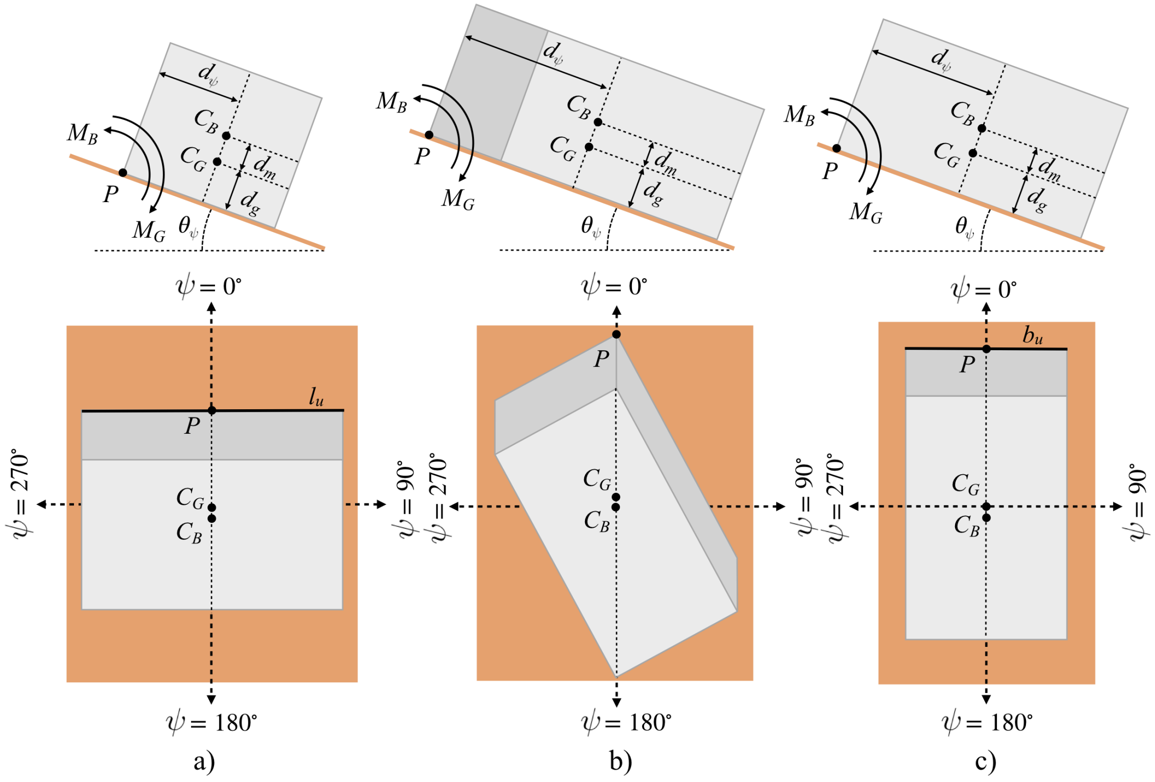

Fig. 7. a) Landing on the slope along the longer edge l_u b) Landing on the slope with the diagonal axis across the slope c) Landing on the slope along the smaller edge b_u

While landing, the vehicle first makes contact with the slope along its smaller edge b_u for orientations $0°$ and $180°$ and longer edge l_u for orientations $90°$ and $270°$. For all other orientations, the vehicle makes contact on one of its corners. To land successfully, the vehicle should settle flush with the slope of the seafloor. Once part of the vehicle makes contact with a sloped seafloor, the vehicle rotates along the plane formed by C_G, C_B and point P as shown in Fig. 7, P being the point where the vehicle makes contact with the seafloor. Since the maximum tilt angle of the vehicle is determined by its righting moment, the maximum angle of rotation is given by the equation

$$\theta_\psi = \tan^{-1}\left[\frac{(d_\psi \times F_R)}{(d_m \times F_B) - (d_g \times F_R)}\right], \tag{1}$$

where the distance d_ψ between the point of contact P and the centre line formed by C_G and C_B is determined by the orientation of the vehicle ψ, with respect to the slope. When landing along an edge, or along a diagonal axis across the slope, as seen in Fig. 7, the vehicle can make full contact with the surface while tilting along a single axis. For all other orientations, the vehicle rotates along a single axis until one of its edges makes contact with the slope after which it rotates about that edge to make full contact with the surface.

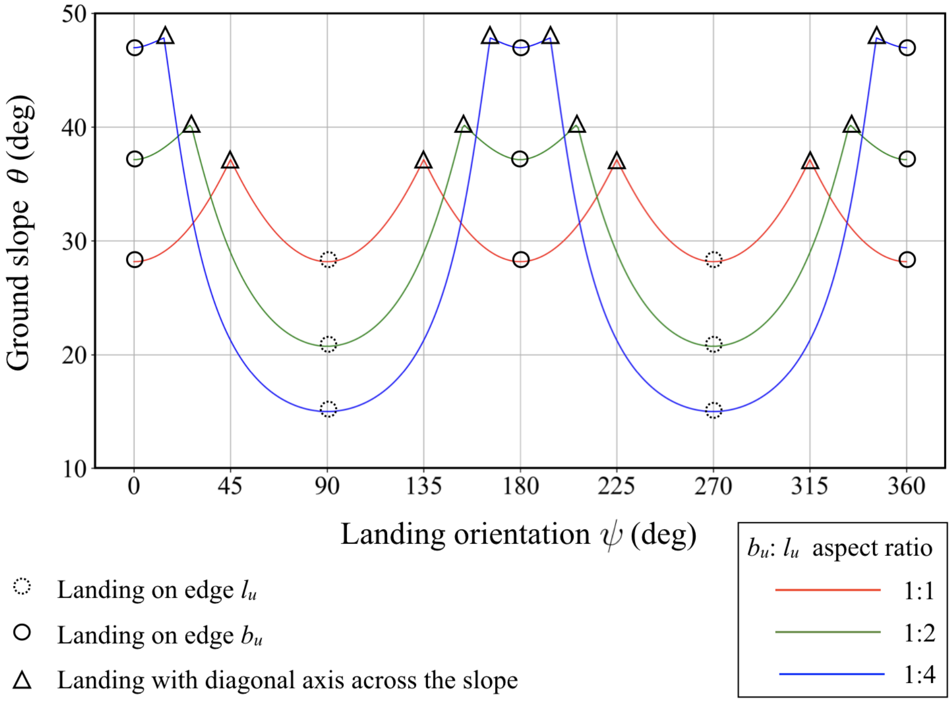

Fig. 8. Maximum landing slope θ_c calculated for different landing orientations and aspect ratios of the vehicle

Fig. 8 shows the maximum slope θ_c where the landing criteria can be met along relative vehicle orientations ψ from $0°$ to $360°$. Simulations are performed for vehicle aspect ratios (l_u/b_u) of 1, 2 and 4 respectively, where the height of the vehicle, distances d_m and d_g and net downwards force F_R remain unchanged. Since the minimum value of θ_c occurs when then vehicle lands on its longer edge l_u, the maximum slope θ_c on which the vehicle can land can be determined by letting $d_\psi = 0.5 \times b_u$ in Equation 1, giving

$$\theta_c = \tan^{-1}\left[\frac{(0.5 \times b_u \times F_R)}{(d_m \times F_B) - (d_g \times F_R)}\right]. \tag{2}$$

For the vehicle parameters in Table II, this gives a maximum slope on which the vehicle can land at any orientation of $\theta_c = 17.7°$.

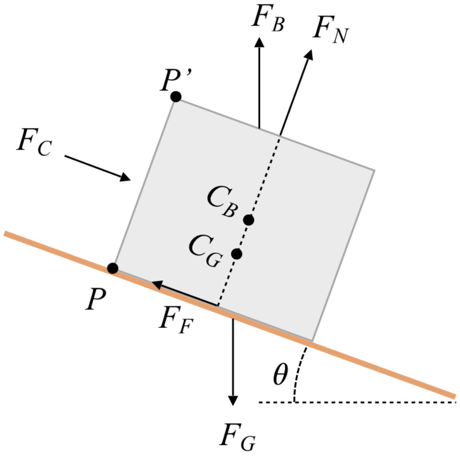

Fig. 9. Forces acting on the vehicle after landing on the sloping surface

For the vehicle to remain stationary on a slope once it has landed, the frictional force F_F needs to be greater than or equal to the sum of the component of gravity F_G acting along the slope in the downwards direction and the force due to seafloor currents F_C pushing the vehicle down the slope, corresponding to $0 < \theta < \pi/2$ (when $\sin\theta$ is positive). Fig. 9 illustrates this worst case scenario, where for the purpose of this simulation we neglect the effects of hydrodynamic lift. The steepness of the slope that the vehicle can remain stationary on depends on the frictional coefficient μ between the vehicle and seafloor. The relationship between the velocity of seafloor currents v and the maximum slope on which the vehicle does not slip with its longer edge l_u across the slope is calculated for a drag coefficient for rectangular shapes $C_d = 1.2$ [33][34] and density $\rho = 1025$ Kg/m^3. The balancing forces for the vehicle to remain stationary after landing can be represented as,

$$F_C - F_F + (F_G - F_B) \times \sin\theta \leq 0 \tag{3}$$

$$F_F = \mu \times (F_G - F_B) \times \cos\theta \tag{4}$$

Giving the force acting on the vehicle due to seafloor currents as,

$$F_C \leq (F_G - F_B) \times (\mu\cos\theta - \sin\theta) \tag{5}$$

The admissible velocity v_c of seafloor currents can be then calculated as:

$$v_c \leq \sqrt{\frac{2 \times F_C}{C_d \times \rho \times l_u \times h_u}} \tag{6}$$

The frictional coefficient of the seafloor typically varies between 0.1 and 0.6 [35] with seafloor currents in the deep ocean typically $< 0.2\,\text{m/s}$ [36]. The effects of friction and current on landing are calculated for slopes between $0°$ and $35°$. The slope values calculated can be seen in Fig. 10 where the area under each curve represents the conditions where the vehicle remains stationary.

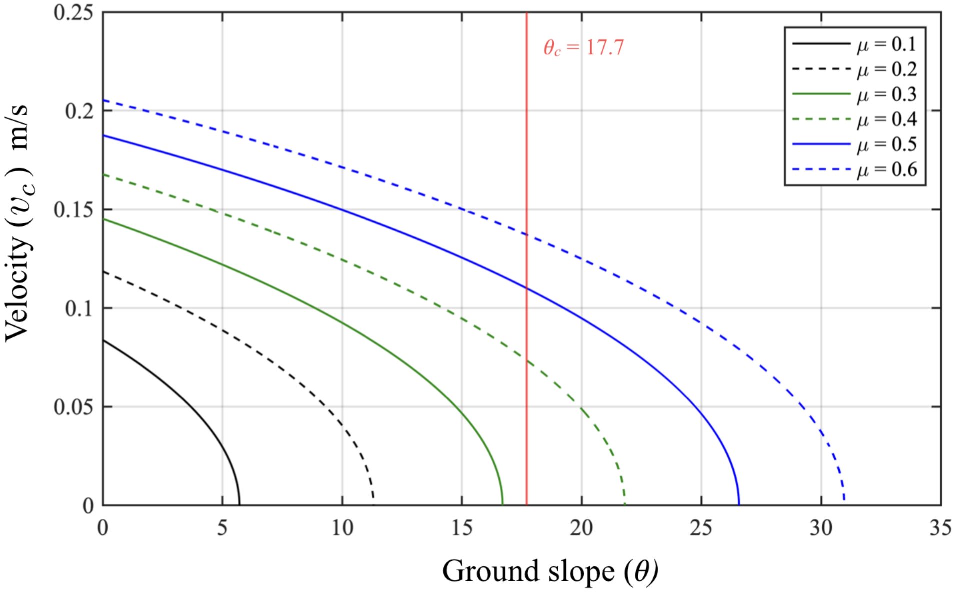

Fig. 10. Analysis of seafloor currents and friction on the ground slope

For a slope of $\theta_c = 17.7°$ determined for the vehicle in Table II, it can be seen that the vehicle will remain stable for currents under 0.14 m/s and coefficient of friction more than 0.32, which is reasonable for most deep-sea applications.

Seafloor protrusions: Seafloor roughness can have an impact on landing. In particular, protrusions can cause a vehicle to remain partially suspended due to its righting moment. Here we consider the criteria for safe landing to be where the vehicle can settle on the seafloor without being limited by its righting moment.

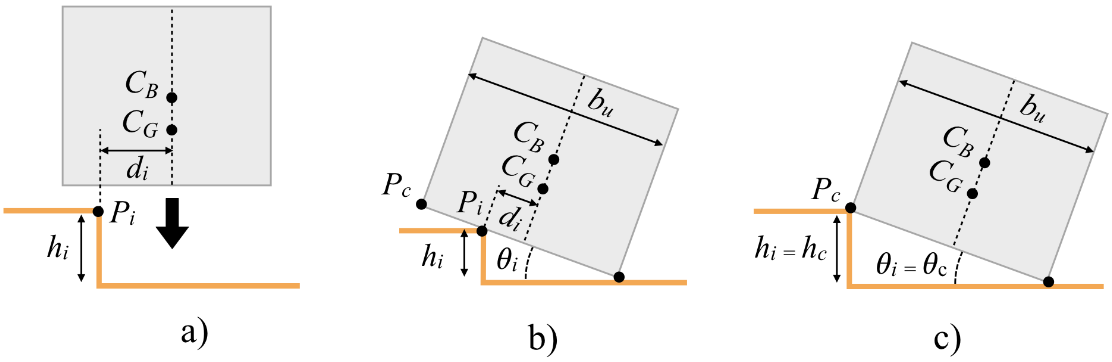

Fig. 11. a) Vehicle landing on an protrusion on the seafloor b) Landing on a protrusion between the edge of the vehicle and the C_G-C_B centre line c) Extreme condition of landing on a protrusion at the edge of the vehicle

Fig. 11a shows a situation where the vehicle lands on the edge of a protrusion P_i at a distance d_i from the C_G. For any protrusion P_i between P_c and the C_G-C_B centre line (Fig. 11b), the maximum angle θ_i to which the vehicle can tilt after making contact is determined by its righting moment, given by the equation 1 as,

$$\theta_i = \tan^{-1}\left[\frac{(d_i \times F_R)}{(d_m \times F_B) - (d_g \times F_R)}\right]. \tag{7}$$

Stability is achieved when the vehicle can make contact with the seafloor after tilting at this angle. The maximum possible height of the protrusion h_i for safe landing after making contact at protrusion P_i can be calculated as,

$$h_i = (0.5 \times b_u + d_i) \times \sin\theta_i. \tag{8}$$

In the extreme condition (Fig. 11c), the vehicle lands along its long edge l_u on point P_c of the protrusion. In this scenario, the condition is identical to the slope condition, with $\theta_i = \theta_c$ forming the limiting condition. The maximum height of the protrusion h_c in this limiting condition can be calculated as:

$$h_c = b_u \times \sin\theta_c \tag{9}$$

To achieve stable landing, any part of the vehicle should be prohibited from landing on protrusions above the height of h_c. For smaller protrusions of height h_i, the C_G of the vehicle should not be allowed to land within a distance d_i from the protrusion depending on the height of the protrusion.

2) Determining landing exclusion zone: The algorithm identifies landing area in the mapped bathymetry by generating an exclusion zone where the C_G of the vehicle cannot enter for landing along any landing heading α using conditions identified in III-B1 as:

- Conditions for landing on sloping surfaces from Equations 2 and 6 to generate an exclusion zone for areas of the seafloor with slope more than θ_c.
- Conditions for landing on protrusions from Equations 7, 8 and 9 to generate an exclusion zone around protrusions on the seafloor based on their height.

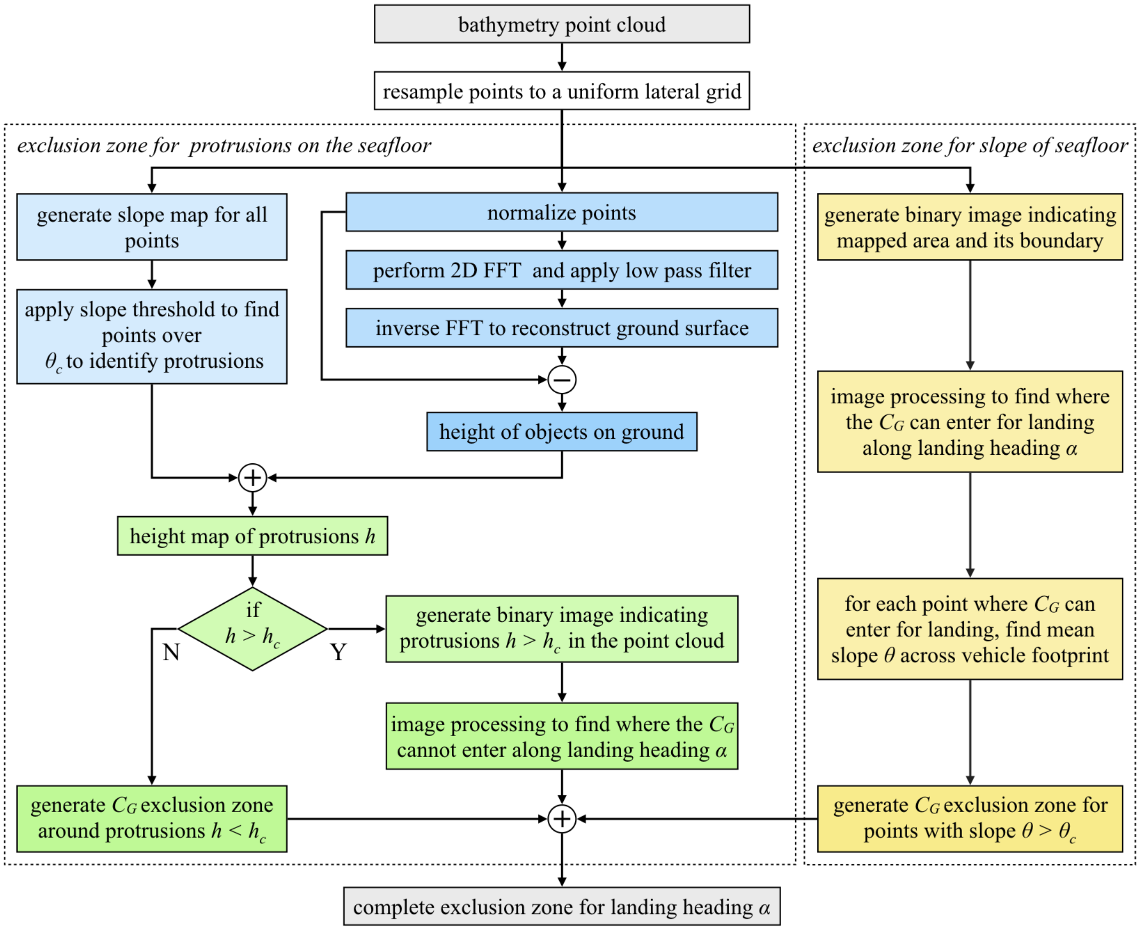

Fig. 12. Flowchart for detection exclusion zone in mapped bathymetry

The approach is summarized in Fig. 12 for the vehicle parameters given in Table II, with the various components described in the following sections. Detailed analysis has been shown for a landing heading $\alpha = 55°$ as an example, which is approximately opposite to the heading of the vehicle during mapping.

Exclusion zone for slope of the seafloor: The point cloud is analysed to generate an exclusion zone for areas with slope more than θ_c where the C_G of the vehicle cannot enter for landing. For this, at first a binary image representing the mapped area and its unmapped boundary is generated as in Fig. 13a. Binary image morphological operations are performed on this image using a structural element with dimensions of the vehicle for a landing heading of $\alpha = 55°$ to generate a map where the C_G of the vehicle can enter for landing as shown in Fig. 13b. The mean slope of the ground over the footprint of the vehicle for each point where the C_G of the vehicle can enter for landing is calculated as in Fig. 13c. A threshold of $\theta_c = 17.7°$ is applied to identify the C_G exclusion zone for slope of the seafloor as seen in Fig. 13d.

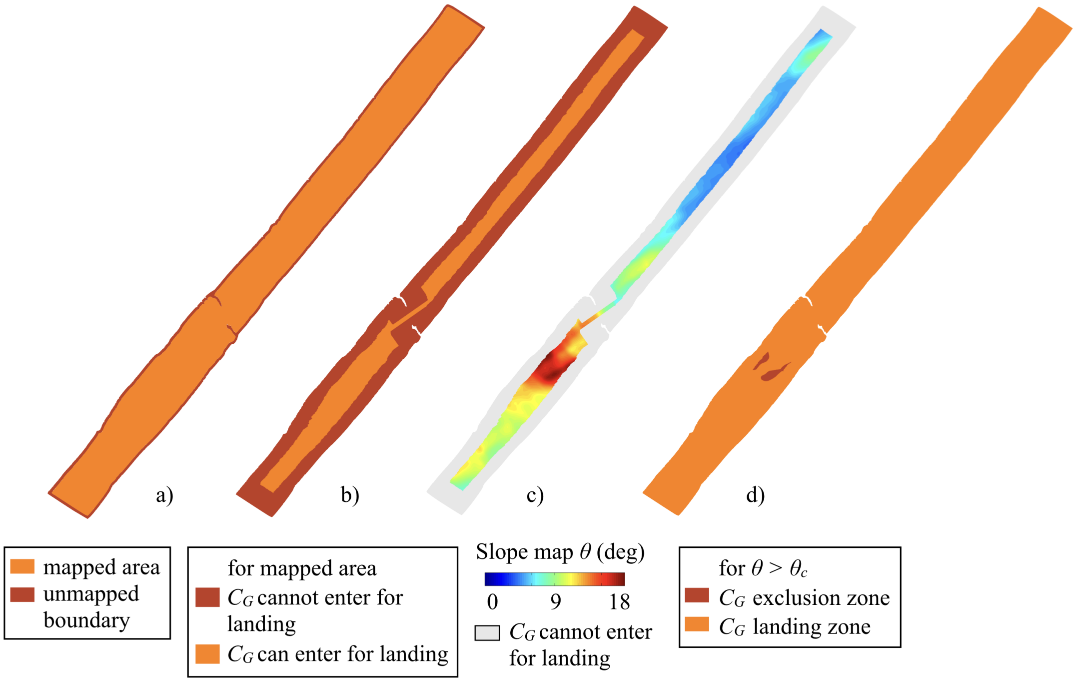

Fig. 13. a) Mapped area and its unmapped boundary b) Binary image showing area where the C_G of vehicle can enter for landing heading of 55° c) Slope map θ for vehicle footprint at landing heading of 55° d) C_G Exclusion zone for slope $\theta > \theta_c$

Exclusion zone for protrusions on the seafloor: An exclusion zone e_i is defined around each protrusion P_i where the C_G of the vehicle cannot enter for landing, as shown in Fig. 14. For the vehicle in Table II, the maximum protrusion height is determined using Equation 9 to be $h_c = 0.15$, where for protrusions higher than h_c, the C_G exclusion zone is set to half the length of the vehicle along a given landing heading α. This prevents the vehicle in this heading from making contact with the protrusion. For protrusions with height $h_i \leq h_c$, the exclusion zone is the distance d_i around the protrusion where the C_G of the vehicle is not allowed to land based on Equations 7 and 8. The height of protrusions is calculated for distances d_i in steps of 5 mm from the C_G-C_B centre line, similar to the mapping resolution, to produce Fig. 15 used for applying the exclusion zone. Protrusions < 5 mm are not considered as protrusions since they cannot be distinguished from noise.

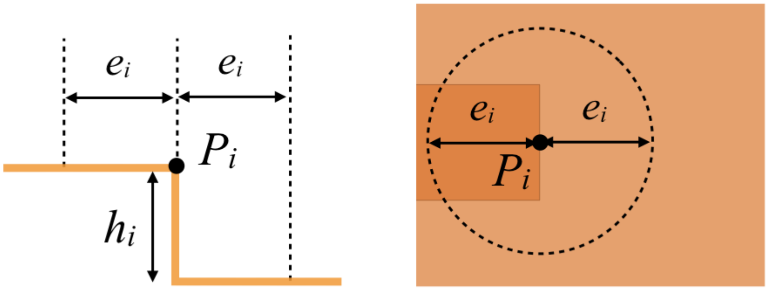

Fig. 14. C_G exclusion where the centre of gravity C_G of the vehicle is prohibited from landing

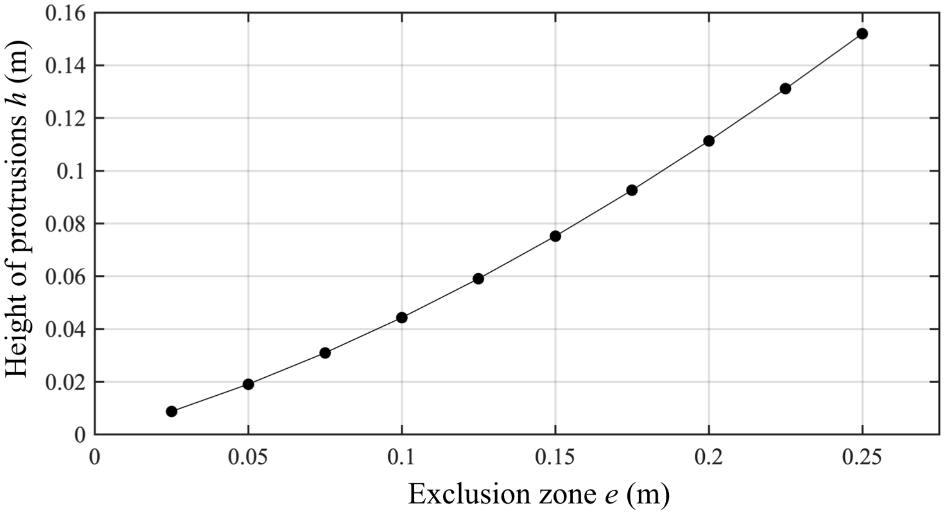

Fig. 15. Exclusion zone for height of protrusions

To identify protrusions in the mapped point cloud, a slope map is generated as shown in Fig. 16a for the three areas A, B and C. Since the vehicle can land on areas with slope less the θ_c, neighbouring points with slope less than this are not considered as protrusions. The slope threshold $\theta_c = 17.7°$ is applied to generate the binary map Fig. 16b to identify protrusions whose height is further analysed.

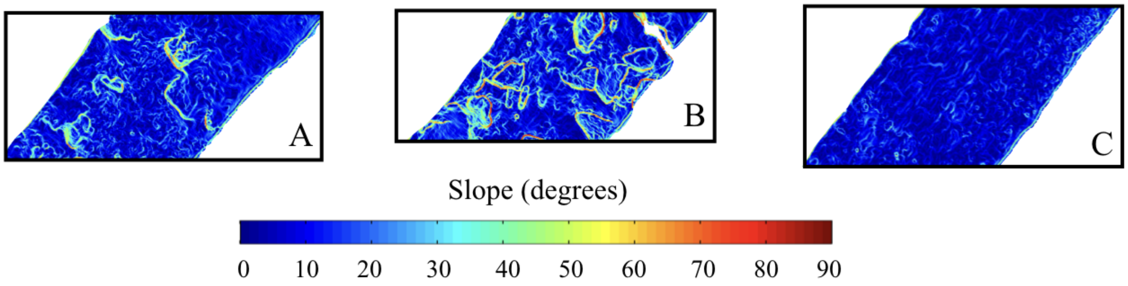

(a) Slope calculated for areas A, B and C. Area B has more inclined slopes than areas A and C. Area C shows smoother surface with gentle slope

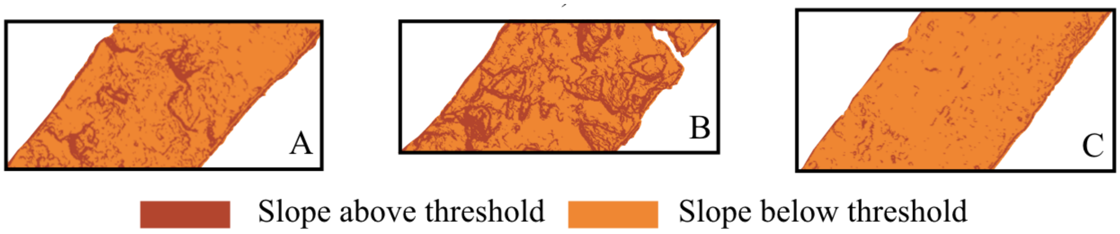

(b) Slope threshold applied to the three areas to generate the binary map of protrusions

Fig. 16. Identifying protrusions in the mapped point cloud

To detect height of protrusions, two dimensional Fourier analysis is performed on the uniformly resampled bathymetry. The points to be analysed are zero filled on all sides to form an $N \times N$ matrix, where N is the next power of 2 more than the largest dimension of the area. The depth values of the points are normalized to remove the zero frequency component by subtracting the mean depth and aligning the points with their Eigenvectors. A two dimensional N point Fast Fourier Transform (FFT) is performed on the normalized values to convert them to the frequency domain. The frequency bins are $n \times f_s/N$, where $n = 1, 2, \ldots, N/2$ and sampling frequency is $f_s = 1/g_{res}$, for grid resolution g_{res}. For a cut-off frequency f_c, filter order n and frequency bins f, a low pass filter is applied as,

$$h_l(f) = \frac{1}{\sqrt{1 + (\frac{f}{f_c})^{2n}}}. \tag{10}$$

A 3rd order filter is used to provide suitable sharpness of damping with 3 dB attenuation at the cut-off frequency. This was determined using the method described in [37] [38] as $f_c = 2/\sigma$, where σ is taken as the diagonal length of the vehicle's geometry as a multiple of the sampling resolution. The filter function is rotated around the zero frequency to form an $N \times N$ point filter and multiplied to the frequency domain values element by element. An inverse two dimensional FFT produces a smooth surface representing the low frequency component. This is subtracted from the unfiltered surface to generate a map of protrusions, as seen in Fig. 17.

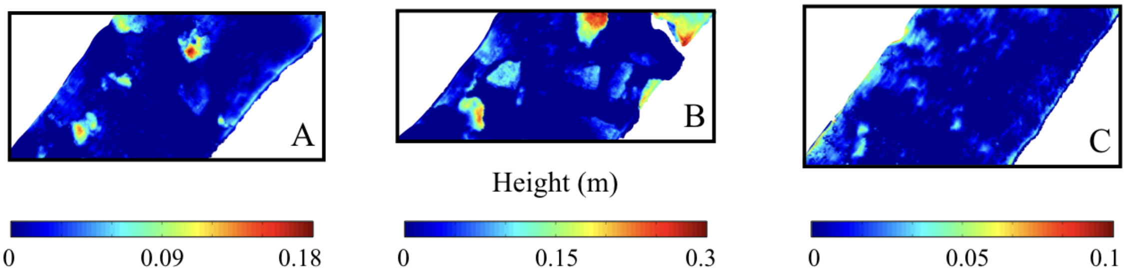

Fig. 17. Height map for areas A, B and C. Areas A and B show large objects on the seafloor compared to area C

The height of protrusions h is extracted in areas above the slope threshold θ_c from the height map of objects as in Fig. 18b. For $h < h_c$, the C_G exclusion zone is generated using the relationship in Fig. 15 giving the C_G exclusion regions shown in Fig. 18c.

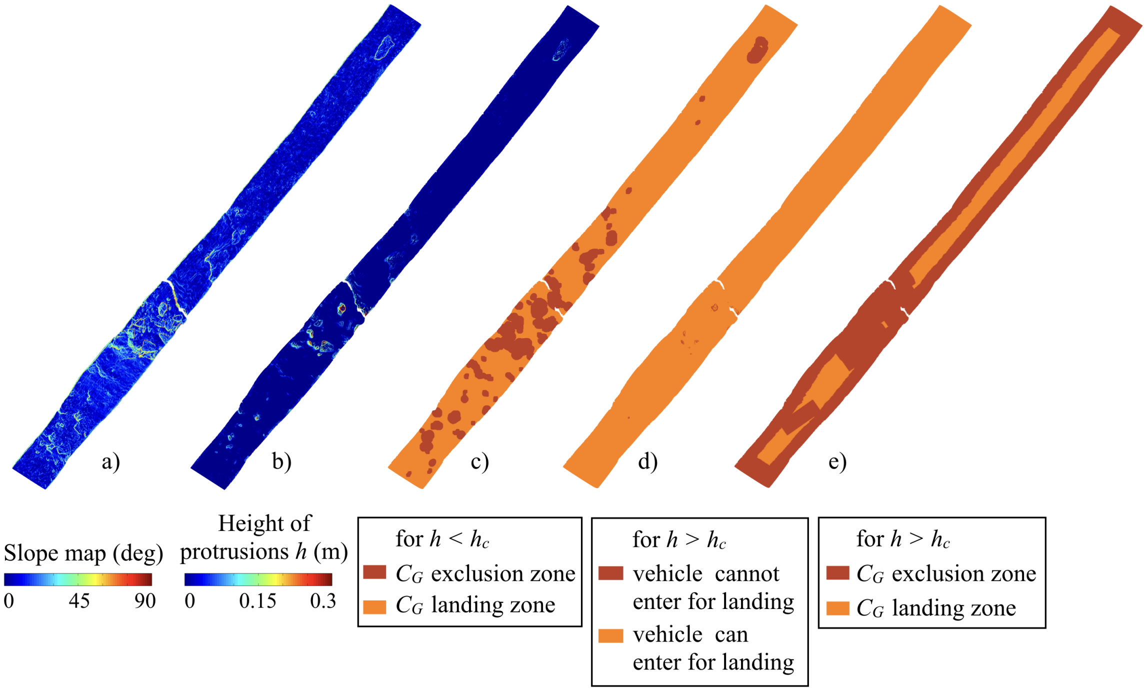

Fig. 18. a) Slope map of the mapped bathymetry b) Height of protrusions h c) C_G exclusion zone for protrusions $h < h_c$ d) Binary image showing protrusions with height $h > h_c$ where the vehicle cannot enter for landing e) C_G Exclusion zone for protrusions $h > h_c$ at 55° landing heading

For protrusions above the threshold $h > h_c$, the C_G exclusion zone takes into account the landing heading α and the geometry of the vehicle such that the vehicle avoids making contact with the protrusion. To achieve this, a binary image representing protrusions where the vehicle cannot enter for landing is generated as in Fig. 18d. Binary image morphological operations are performed on this image using a structural element with the dimensions of the vehicle for the landing heading $\alpha = 55°$ as shown in Fig. 18e.

C. Site identification

The exclusion zones for slope of the seafloor in Fig. 13d and for protrusions in Fig. 18c and Fig. 18e are combined to form the full exclusion zone for that landing heading. The exclusion zone for landing heading of $55°$ is seen in Fig. 19a. Within this, landing sites are identified by verifying the eight neighbor connectivity between pixels where the vehicle C_G can land. A landing coordinate is calculated for each group of pixels where the vehicle can land furthest away from the group's boundary.

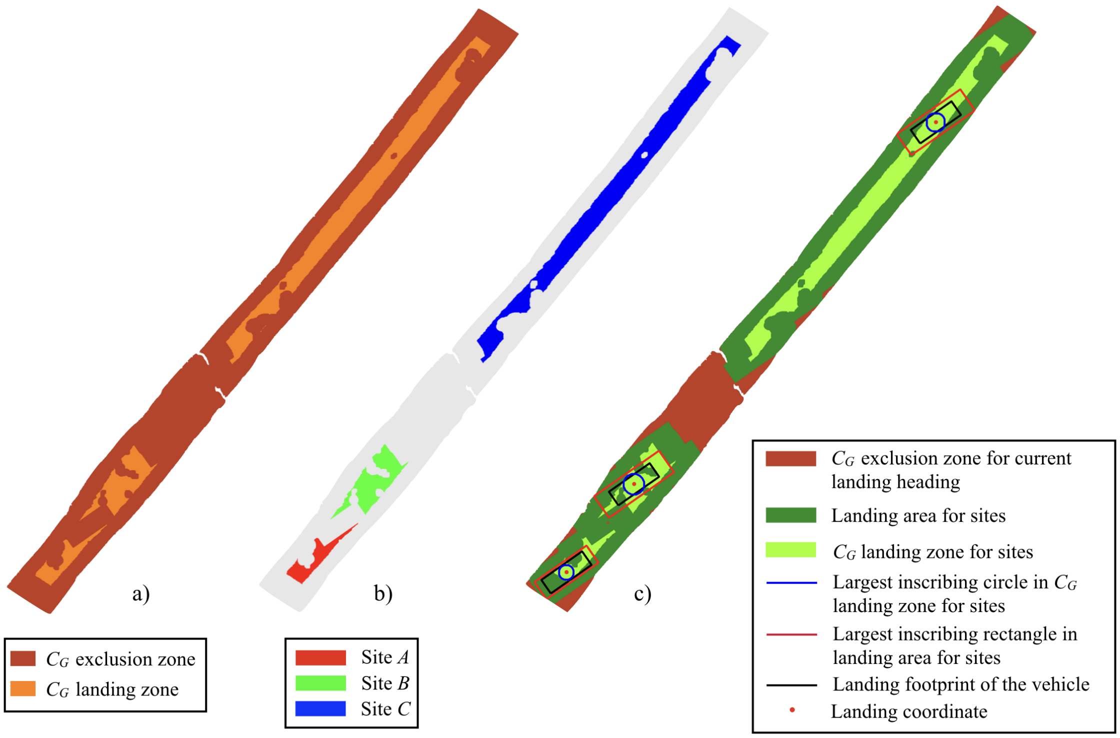

Fig. 19. a) Full C_G exclusion zone for a $55°$ landing heading, b) Landing sites identified for $55°$ landing heading, and c) Landing point calculation

This is achieved by determining the largest circle that can be inscribed within the group of pixels, where the centre of this circle is the landing coordinate. Groups where the radius of the largest inscribed circle is $< 0.3\,\mathrm{m}$ are rejected considering AUV positioning errors when navigating back to each site. The remaining groups are labelled as candidate landing sites, where Fig. 19 shows the candidate sites identified for a vehicle heading of 55°. Each candidate site is characterised by extracting the following seafloor properties from within the footprint of the vehicle for each landing coordinate and heading, as illustrated in Fig. 19c.

- *Slope P_s:* The mean landing slope $\overline{\theta}$ is calculated for the points in the landing footprint of the vehicle. The slope is normalized using the threshold slope θ_c to determine the slope cost as follows,

$$P_s = \frac{\overline{\theta}}{\theta_c}. \tag{11}$$

- *Safety P_f:* Landing safety is determined by calculating the area of the largest rectangle with the same aspect ratio as the vehicle that can be inscribed in the landing site along the landing heading. The ratio of this area A_r to the footprint of the vehicle A_f is used to calculate the safety cost. Since beyond a certain ratio, having a larger area to land does not increase safety, the value of the cost P_f is limited to between 0 and 1 as follows,

$$P_f = \frac{1}{4}\left(5 - \frac{A_r}{A_f}\right) \text{where } 0 < P_f < 1. \tag{12}$$

- *Roughness P_r:* The mean deviation of height of protrusions h (Fig. 18b) from its mean value $\overline{h}$ is used to determine the roughness R for the landing footprint. This is normalized by the maximum value of roughness, R_{max}, which is calculated for the terrain with maximum possible height of protrusions in the landing footprint.To determine this terrain, the maximum height of protrusions around the centre of footprint are determined as in Fig. 20a which will result in the centre being out of the C_G exclusion zone for landing as in Fig. 20b.

$$R = \frac{1}{n}\sum_{i=1}^{n}\left|h_i - \overline{h}\right| \tag{13}$$

$$P_r = \frac{R}{R_{max}} \tag{14}$$

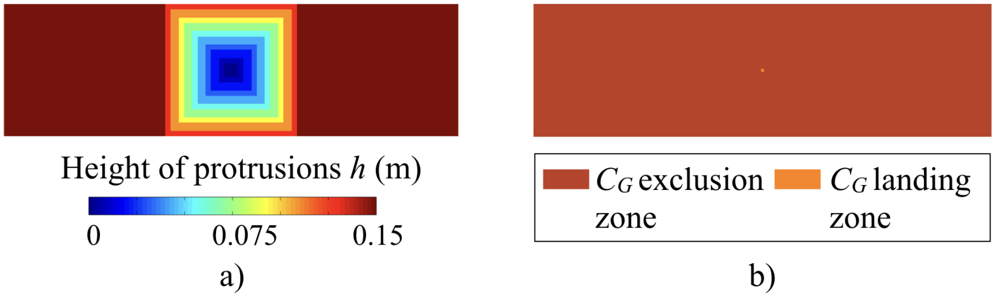

Fig. 20. a) Terrain in the landing footprint with maximum possible height of protrusions resulting in the largest roughness, R_{max} b) C_G exclusion zone calculated for this terrain with centre of the footprint out of the exclusion zone for landing

D. Site selection

In order to select the most suitable landing site, the following cost function is defined based on the features of each candidate site,

$$C_s = \frac{1}{3}\left[P_s + P_f + P_r\right]. \tag{15}$$

The candidate site with the lowest cost is selected as the most suitable landing site. The landing costs calculated for the three sites in Fig.19c are shown in Table III, where in this case site C is the most suitable of the three candidates.

TABLE III

LANDING SITE PROPERTIES

Site	P_s	P_f	P_r	C_s
A	0.54	0.85	0.29	0.56
B	0.67	0.62	0.32	0.54
C	0.34	0.65	0.15	0.38

For each section of mapped bathymetry, the most suitable landing site is selected from candidate sites determined for multiple landing headings. These are calculated between $-90°$ and $90°$, where the costs for landing sites in the opposite direction are identical for a rectangular vehicle geometry. Costs are calculated in steps of $5°$ to achieve a balance between resolution and computational cost.

The landing costs calculated for all the landing candidates in the bathymetry shown in Fig. 4 are plotted in Fig. 21. The analysis shows that landing site C for a landing heading of $\alpha = 40°$

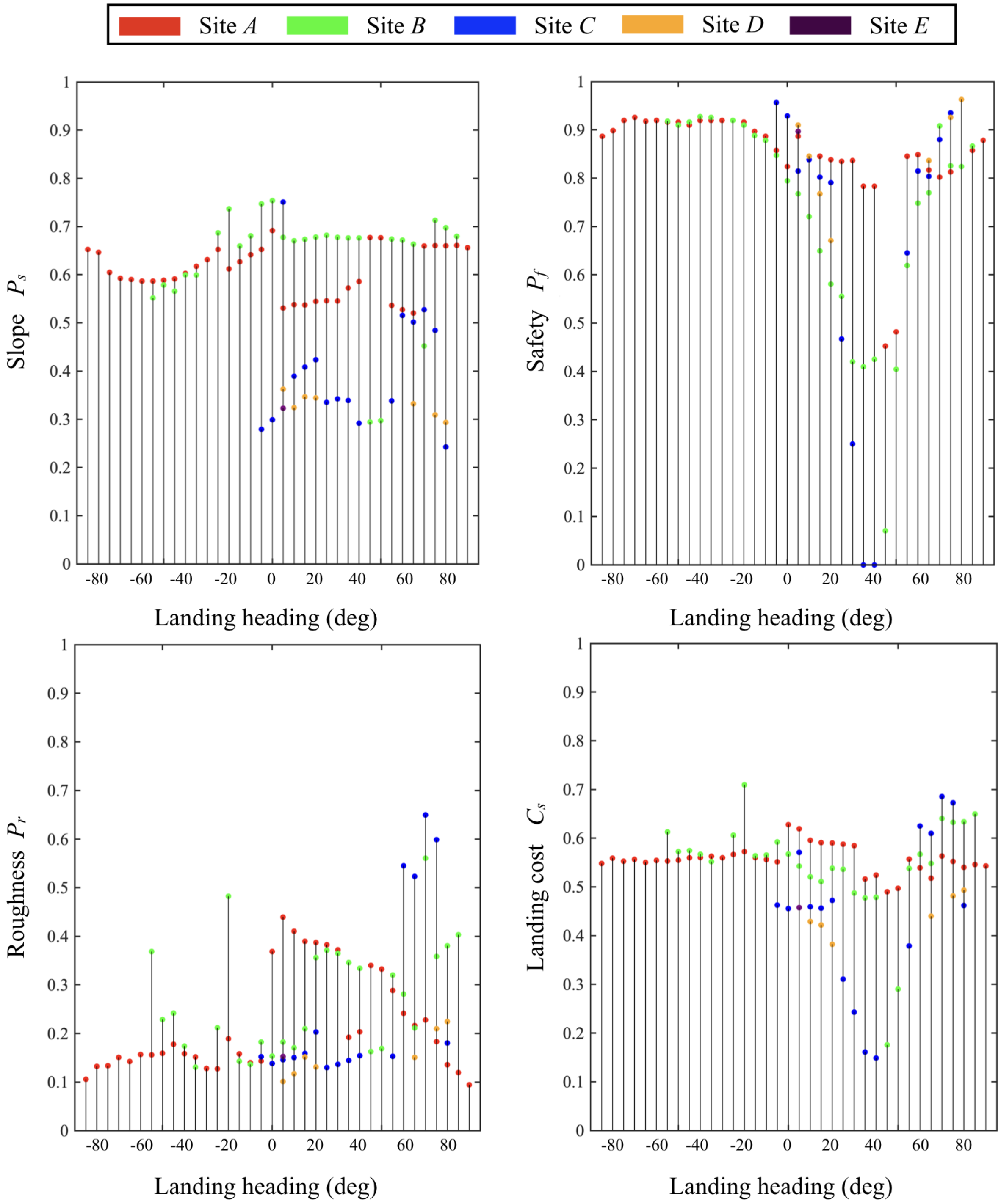

Fig. 21. Properties of landing sites between landing headings $-90°$ and $90°$ in steps of $5°$

has the lowest cost and is selected as the final landing site in this region of seafloor, with the properties of the site shown in Table IV.

TABLE IV

PROPERTIES FOR FINAL LANDING SITE

Property	**Value**
Landing heading	40°
Mean depth	1379.7 m
P_s	0.29
P_f	0.00
P_r	0.16
C_s	0.15

IV. IMPLEMENTATION ON SEAFLOOR DATA

The landing algorithm is applied to a 500 m section of high resolution seafloor laser bathymetry data collected on the southern slopes of the Takuyo Daigo seamount between depths of 1379 and 1429 m. The data was obtained by the AUV BOSS-A using the same mapping system described in Section III. In order to perform the analysis, the data is split into twenty 25 m long submaps as illustrated in Fig. 22.

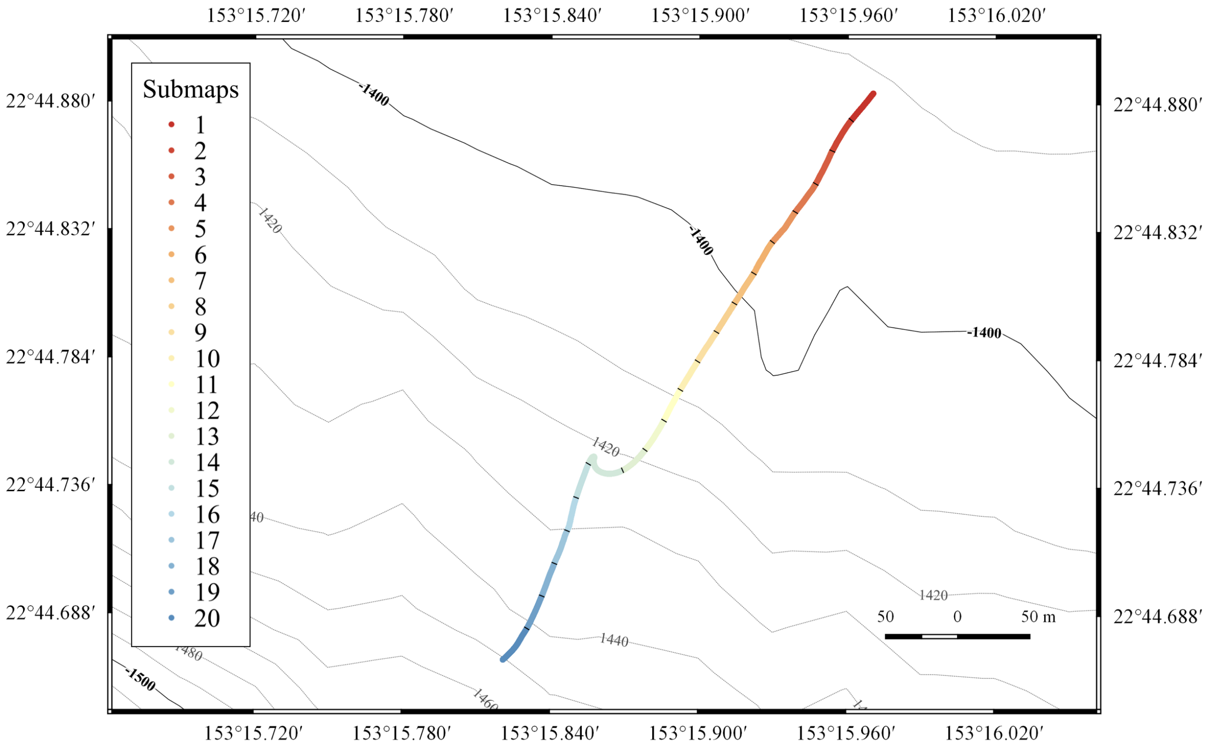

Fig. 22. Vehicle trajectory at Takuyo Daigo seamount where the algorithm is implemented on twenty 25 m long submaps

The northern part of the transect (submaps 1 to 9) is gently sloped with relatively flat, exposed manganese crusts. The southern parts of the transect (submaps 10 to 20) is more steeply sloped with a higher degree of roughness [18], [21]. The algorithm was applied to determine the most appropriate landing coordinate and heading within each submap for the vehicle parameters given in Table II. The algorithm found at least one landing sites in each submap with a total of 754 landing sites, the landing cost details of which are shown in Table V.

TABLE V

RESULTS OF ANALYSIS ON MAPPED BATHYMETRY

Property	**Value**
Transect length	521 m
Area surveyed	794.4 sq.m.
Number of sites	754
Mean landing cost	0.28
Landing cost range	$0.15 - 0.63$
Landing cost Std. Dev.	0.13

The properties of the final landing site with the least landing cost in each submap can be seen in Fig. 23a. The landing heading for each submap is close to the mapping heading due to the narrow swath of the bathymetry as shown by Fig. 23b. The narrow swath of the bathymetry is clearly visible for the submaps shown in Fig. 24. The sites towards the south of the transect (submaps 10 to 20) have higher landing costs than the sites towards the north of the transect (submaps 1 to 9) with larger values of P_s and P_r due to the increased steepness and roughness of the seafloor. Fig. 24a shows submap 1, which has a low landing cost due to the wide swath and gently sloping smooth surface. Submap 13 (Fig. 24b) shows a narrow landing area due to reduced mapping swath while turning on a smooth, gently sloping area of the seafloor. Submap 20 (Fig. 24c) towards the lower end of the transect has a narrow landing area on an area with high roughness and a steep slope, resulting in a high landing cost. Fig. 25 shows the locations of each landing site identified in the submaps with their C_s values.

The algorithm was implemented in MATLAB R2018 and executed on a computer, the specifications of which are given in Table VI. Parallel processing was not used for this implementation and the algorithm was run using a single CPU thread. Each 25 m submap takes the vehicle about 250 seconds to record raw images and position data at a forward velocity of 0.1 m/s. The

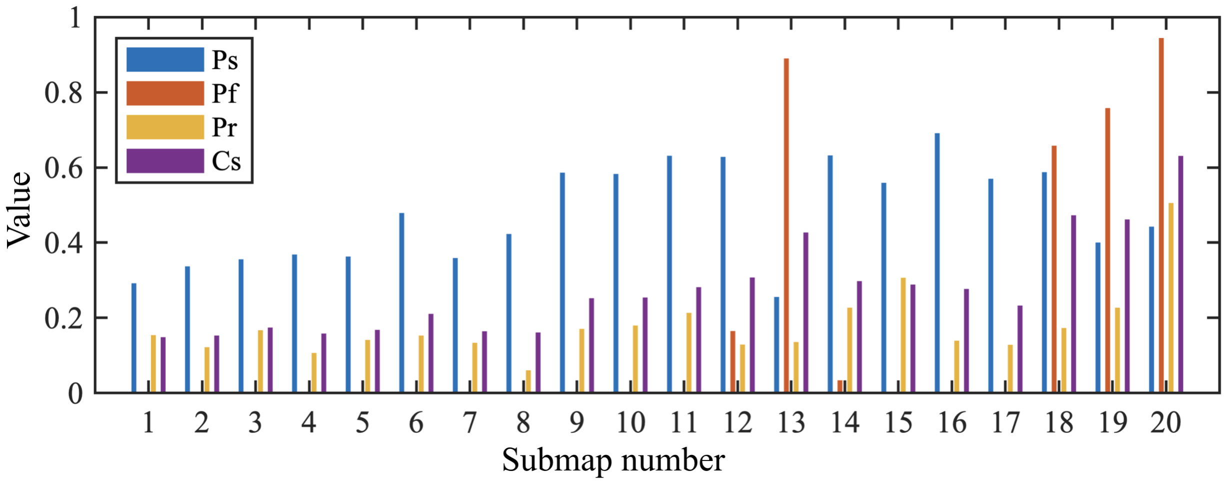

(a) Properties and landing costs determined for the sites selected within each submap

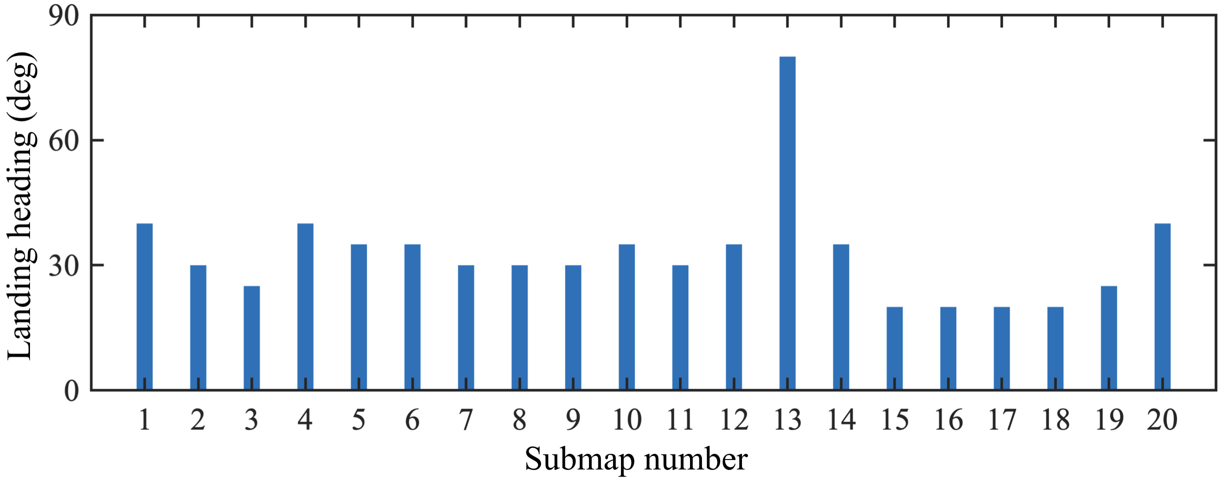

(b) Landing headings for the sites selected within each submap

Fig. 23. Characteristics of the landing sites determined by the algorithm for the submaps analysed in this work.

program to convert the raw data into a bathymetry point cloud is implemented in C++ [21] and takes an average of 33.5 sec to execute for a submap.

Each submap is split into an average of 14 blocks of 2.5 m mapping transect length to generate slope maps and height of protrusion maps for the blocks. The individual maps generated for all the blocks are then combined to make full maps for the submap. An exclusion zone is calculated using these full maps for landing headings between -90° and 90° in steps of 5° followed by landing site identification and final landing site selection. The average computation time for different steps of the algorithm for all submaps is also seen in Table VI. The processes for generation of individual maps for blocks and identification of landing sites for different landing

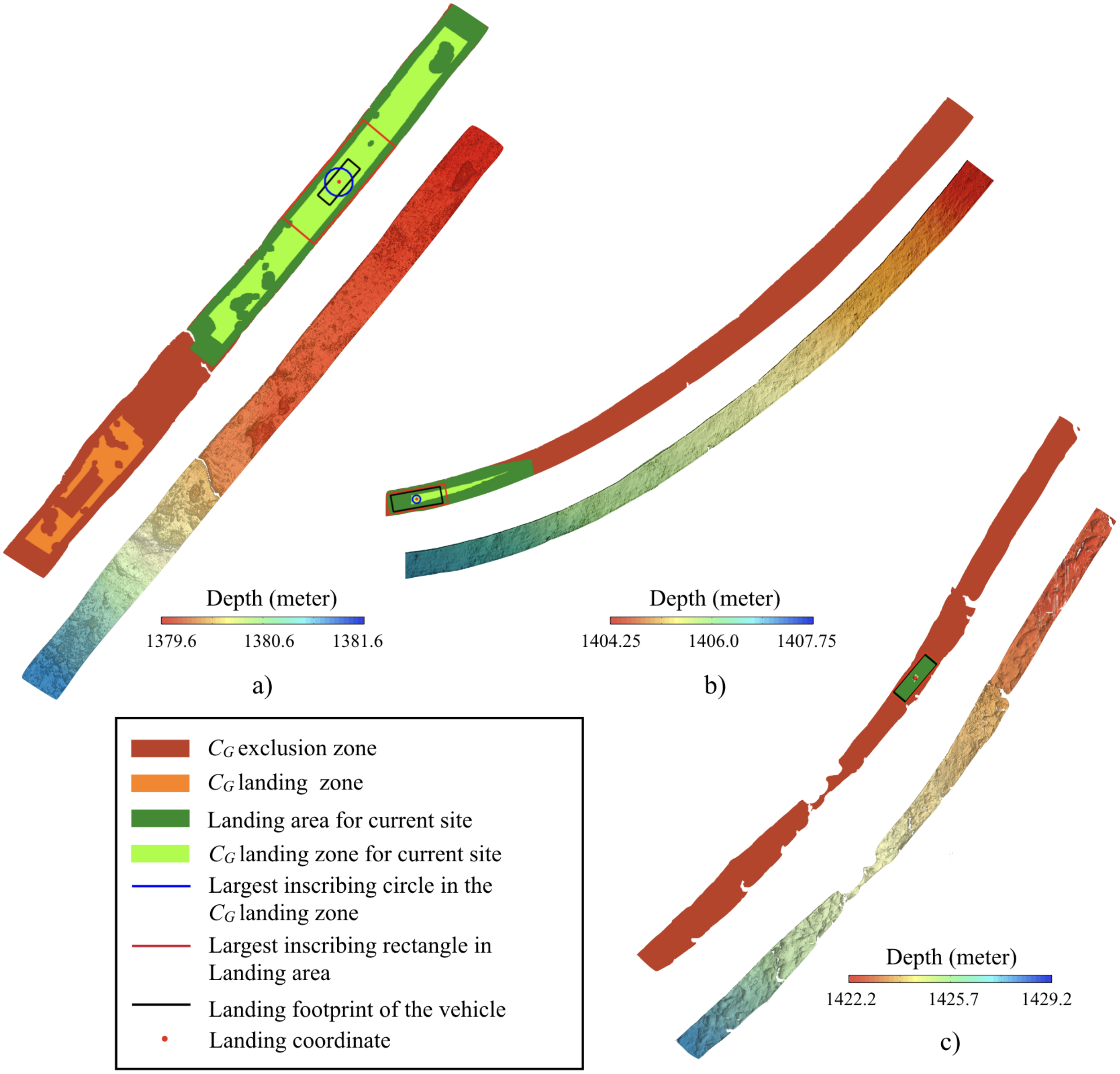

Fig. 24. Landing coordinate detected for a) Submap 1 at start of the transect on a gently sloping smooth surface b) Submap 13 towards the middle of the transect with narrow mapping swath c) Submap 20 at the end of the transect on a steep sloping rough surface

headings can be executed in parallel since they are independent and not memory intensive. This can reduce the overall computation time of the algorithm for execution during seafloor surveys.

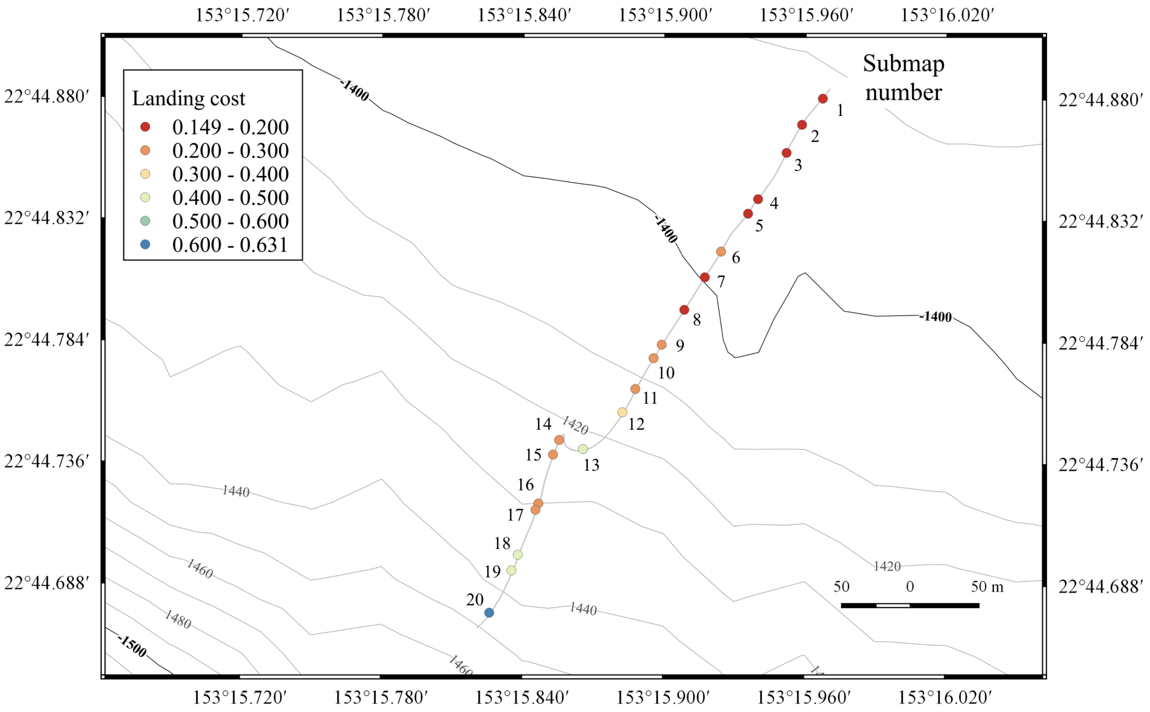

Fig. 25. Landing costs for identified final landing sites for submaps in the transect

V. CONCLUSIONS

- This paper has described vehicle hardware and seafloor mapping system considerations specific to autonomous landing, together with the concept of a negatively buoyant, fast transiting landing vehicle using wing sections.
- A novel, fully automated method to identify safe landing sites for an AUV based on mm-resolution seafloor bathymetry has been developed and demonstrated based on data collected during field operations.
- The conditions for safe landing have been derived, taking into consideration the seafloor slope, protrusions and vehicle geometry.
- An algorithm to identify and rank potential landing sites (location and heading) has been developed and its effectiveness demonstrated on a 500 m transect of seafloor data acquired using high resolution laser mapping system.
- The described method can allow autonomous platforms to land safely, where the computations required for the algorithm can be completed in dive relevant time frames, as demonstrated using a standard mid-range CPU.

TABLE VI

COMPUTER SPECIFICATIONS AND COMPUTATION TIMES

Specification	**Value**
Processor	Intel Core i7
Processor speed	2.2 GHz
RAM	16 GB
Graphics card	Intel Iris Pro 1536 MB
Number of threads	1
Software	MATLAB R2018

Process	**Subprocess**	**Time (sec)**
Processing raw points		
	Resampling to lateral uniform grid	**14.1**
Processing one block		
	Generate slope map	0.2
	Normalize points	0.1
	FFT and smoothing	1.7
	Generate protrusion height map	0.2
Processing for submap		
	Generating maps for 14 blocks	**30.8**
	Combining blocks to full maps	**6.7**
	Generate exclusion zone for protrusions $h < h_c$	**4.3**
Landing sites for one landing heading		
	Generate exclusion zone for slope	1.8
	Generate exclusion zone for protrusions $h > h_c$	1.1
	Identify landing sites	0.1
	Generate landing site properties	2.5
Final landing site for submap		
	Landing sites for headings between $-90°$ and $90°$ in steps of $5°$	**198**
	Final landing site selection	**1.0**
Total time for submap		**254.9**

ACKNOWLEDGMENTS

The authors would like to thank Y. Nishida of Kyushu Institute of Technology, K. Nagahashi and K. Nagano of Mitsui Engineering and Shipbuilding, U. Neettiyath of The University of

Tokyo and T. Koike of Kaiyo Engineering for their help in deployment of BOSS-A during the KR16−01 cruise of R/V Kairei. This work was funded under the Program for the Development of Fundamental Tools for the Utilization of Marine Resources of the Japanese Ministry of Education.

REFERENCES

[1] K. Suzuki, J. Ishibashi, Y. Kato, and T. Nozaki, "Preface: Front edge of submarine mineral resources research in japan," *Geochemical Journal*, vol. 49, no. 6, pp. 575–577, 2015.

[2] A. Usui, K. Nishi, H. Sato, Y. Nakasato, B. Thornton, T. Kashiwabara, A. Tokumaru, A. Sakaguchi, K. Yamaoka, S. Kato, S. Nitahara, K. Suzuki, K. Iijima, and T. Urabe, "Continuous growth of hydrogenetic ferromanganese crusts since 17 myr ago on takuyo-daigo seamount, nw pacific, at water depths of 800 to 5500 m," *Ore Geology Reviews*, vol. 87, pp. 71–87, 2017.

[3] T. Schoening, T. Kuhn, D. O. Jones, E. Simon-Lledo, and T. W. Nattkemper, "Fully automated image segmentation for benthic resource assessment of poly-metallic nodules," *Methods in Oceanography*, vol. 15, pp. 78–89, 2016.

[4] B. Thornton, A. Bodenmann, O. Pizarro, S. B. Williams, A. Friedman, R. Nakajima, K. Takai, K. Motoki, T. Watsuji, H. Hirayama, Y. Matsui, H. Watanabe, and T. Ura, "Biometric assessment of deep-sea vent megabenthic communities using multi-resolution 3d image reconstructions," *Deep-Sea Research Part I: Oceanographic Research Papers*, vol. 116, pp. 200–219, 2016.

[5] C. De Moustier and H. Matsumoto, "Seafloor acoustic remote sensing with multibeam echo-sounders and bathymetric sidescan sonar systems," *Marine Geophysical Researches*, vol. 15, no. 1, pp. 27–42, 1993.

[6] C. Roman, G. Inglis, and J. Rutter, "Application of structured light imaging for high resolution mapping of underwater archaeological sites," in *OCEANS 2010 IEEE - Sydney*, 2010, pp. 1–9.

[7] O. Pizarro, S. B. Williams, and J. Colquhoun, "Topic-based habitat classification using visual data," in *OCEANS 2009 - EUROPE*. IEEE, 2009, pp. 1–8.

[8] T. Maki, A. Kume, T. Ura, T. Sakamaki, and H. Suzuki, "Autonomous detection and volume determination of tubeworm colonies from underwater robotic surveys," in *OCEANS 2010 IEEE - Sydney*. IEEE, 2010, pp. 1–8.

[9] T. Takahashi, B. Thornton, K. Ohki, and T. Sakka, "Calibration-free analysis of immersed brass alloys using long-ns-duration pulse laser-induced breakdown spectroscopy with and without correction for nonstoichiometric ablation," *Spectrochimica Acta Part B: Atomic Spectroscopy*, vol. 111, pp. 8–14, 2015.

[10] D. White and H. Dingle, "The mechanism of steady friction between seabed pipelines and clay soils," *Géotechnique*, vol. 61, no. 12, pp. 1035–1041, 2011.

[11] D. M. Rubin, H. Chezar, J. N. Harney, D. J. Topping, T. S. Melis, and C. R. Sherwood, "Underwater microscope for measuring spatial and temporal changes in bed-sediment grain size," *Sedimentary Geology*, vol. 202, no. 3, pp. 402–408, 2007.

[12] B. Thornton, S. Ohnishi, T. Ura, N. Odano, S. Sasaki, T. Fujita, T. Watanabe, K. Nakata, T. Ono, and D. Ambe, "Distribution of local 137cs anomalies on the seafloor near the fukushima dai-ichi nuclear power plant," *Marine Pollution Bulletin*, vol. 74, no. 1, pp. 344–350, 2013.

[13] B. Thornton, S. Ohnishi, T. Ura, N. Odano, and T. Fujita, "Continuous measurement of radionuclide distribution off fukushima using a towed sea-bed gamma ray spectrometer," *Deep Sea Research Part I: Oceanographic Research Papers*, vol. 79, pp. 10–19, 2013.

[14] B. Thornton, T. Takahashi, T. Sato, T. Sakka, A. Tamura, A. Matsumoto, T. Nozaki, T. Ohki, and K. Ohki, "Development of a deep-sea laser-induced breakdown spectrometer for in situ multi-element chemical analysis," *Deep Sea Research Part I: Oceanographic Research Papers*, vol. 95, pp. 20–36, 2015.

[15] P. G. Brewer, G. Malby, J. D. Pasteris, S. N. White, E. T. Peltzer, B. Wopenka, J. Freeman, and M. O. Brown, "Development of a laser raman spectrometer for deep-ocean science," *Deep Sea Research Part I: Oceanographic Research Papers*, vol. 51, no. 5, pp. 739–753, 2004.

[16] J. Pasteris, B. Wopenka, J. J. Freeman, G. P. Brewer, N. S. White, T. E. Peltzer, and E. G. Malby, "Raman spectroscopy in the deep ocean: Successes and challenges," *Appl. Spectrosc.*, vol. 58, pp. 195A–208A, 2004.

[17] S. A. Stanier, D. J. White, S. Chatterjee, P. Brunning, and M. F. Randolph, "A tool for rov-based seabed friction measurement," *Physics Procedia*, vol. 50, pp. 155–162, 2015.

[18] B. Thornton, A. Asada, A. Bodenmann, M. Sangekar, and T. Ura, "Instruments and methods for acoustic and visual survey of manganese crusts," *IEEE Journal of Oceanic Engineering*, vol. 38, no. 1, pp. 186–203, jan 2013.

[19] G. Inglis, C. Smart, I. Vaughn, and C. Roman, "A pipeline for structured light bathymetric mapping," in *2012 IEEE/RSJ International Conference on Intelligent Robots and Systems*, 2012, pp. 4425–4432.

[20] Y. Nishida, K. Nagahashi, T. Sato, A. Bodenmann, B. Thornton, A. Asada, and T. Ura, "Autonomous underwater vehicle boss-a for acoustic and visual survey of manganese crusts," *Journal of Robotics and Mechatronics*, vol. 28, no. 1, pp. 91–94, 2016.

[21] A. Bodenmann, B. Thornton, and T. Ura, "Generation of high-resolution three-dimensional reconstructions of the seafloor in color using a single camera and structured light," *Journal of Field Robotics*, vol. 34, no. 5, pp. 833–851, 2017.

[22] V. R. Desaraju, N. Michael, M. Humenberger, R. Brockers, S. Weiss, J. Nash, and L. Matthies, "Vision-based landing site evaluation and informed optimal trajectory generation toward autonomous rooftop landing," *Autonomous Robots*, vol. 39, no. 3, pp. 445–463, 2015.

[23] C. S. Sharp, O. Shakernia, and S. S. Sastry, "A vision system for landing an unmanned aerial vehicle," in *Proceedings 2001 ICRA. IEEE International Conference on Robotics and Automation (Cat. No.01CH37164)*, vol. 2, 2001, pp. 1720–1727.

[24] S. Wang, H. Zhang, W. Hou, J. Liang, P. Taylor, H. Zhangy, W. Houy, and J. Liangz, "Control and navigation of the variable buoyancy auv for underwater landing and takeoff," *International Journal of Control*, vol. 80, no. 7, pp. 1018–1026, 2007.

[25] B. Du, Y. Jiang, and H. Zhang, "Dynamic analysis of landing autonomous underwater vehicle," *Transactions of Tianjin University*, vol. 18, no. 4, pp. 298–304, Aug. 2012.

[26] B. Douillard, N. Nourani-Vatani, M. Johnson-Roberson, S. Williams, C. Roman, O. Pizarro, I. Vaughn, and G. Inglis, "Fft-based terrain segmentation for underwater mapping," in *Proceedings of Robotics: Science and Systems*, Sydney, 2012.

[27] B. Douillard, N. Nourani-Vatani, M. Johnson-Roberson, O. Pizarro, S. Williams, C. Roman, and I. Vaughn, "Frequency-based underwater terrain segmentation," *Autonomous Robots*, vol. 35, no. 4, pp. 255–269, Jul. 2013.

[28] S. H. Bhandari and S. M. Deshpande, "Feature extraction for surface classification - an approach with wavelets," *International Journal of Computer and Information Science and Engine*, vol. 1, no. 4, pp. 322–326, 2007.

[29] M. N. Sangekar, B. Thornton, T. Nakatani, and T. Ura, "Development of a landing algorithm for autonomous underwater vehicles using laser profiling," in *OCEANS'10 IEEE - Sydney*. Sydney, Australia: IEEE, 2010, pp. 1–7.

[30] J. S. Riedel, A. J. Healey, D. B. Marco, and B. Beyazay, "Design and development of low cost variable buoyancy system for the soft grounding of autonomous underwater vehicles," *Naval Postgraduate School, Center for AUV Research*, 2005.

[31] B. Thornton, "Sizing drop weights for deep diving submersibles taking into account non-uniform seawater density profiles," *Journal of Oceanic Engineering*, pp. 1–11, 2019.

[32] L. Paull, S. Saeedi, M. Seto, and H. Li, “Auv navigation and localization: A review,” *IEEE Journal of Oceanic Engineering*, vol. 39, pp. 131–149, 2014.

[33] B. Ferreira, A. Matos, N. Cruz, and M. Pinto, “Modeling and Control of the MARES Autonomous Underwater Vehicle,” *Marine Technology Society Journal*, vol. 44, no. 2, pp. 19–36, 2010.

[34] S. Hoerner, *Fluid-dynamic drag: practical information on aerodynamic drag and hydrodynamic resistance*. Hoerner Fluid Dynamics, 1965.

[35] DNV-RP-F109, “On-bottom stability design of submarine pipelines,” 2017.

[36] C. D. Hollister and B. C. Heezen, “Geologic effects of ocean bottom currents - western north atlantic,” *In Gordon, A. L., ed., Studies in physical oceanography New York, Gordon & Breach*, vol. 2, pp. 37–66, 1972.

[37] Lyons Richard G., *Understanding digital signal processing*. Addison Wesley Pub. Co Reading, Mass, 1997.

[38] E. Kalogerakis, A. Hertzmann, and K. Singh, “Learning 3D mesh segmentation and labeling,” *ACM Transactions on Graphics*, vol. 29, no. 4, p. 1, 2010.

Sangekar Mehul Naresh (M10) received the M.Sc. degree in underwater robotics and Ph.D. degree in ocean technology from The University of Tokyo, Japan, in 2010 and 2014, respectively. He is working at present as a project researcher at the Thornton Lab, Institute of Industrial Science, The University of Tokyo. Currently, he works on techniques for intelligent, multi-layer resolution mapping of the seafloor using autonomous underwater vehicles. He is also working on developing algorithms for analysis of high resolution seafloor bathymetry and correlating it with other measured seafloor parameters.

Thornton Blair (M07) received the B.Eng. degree in ship science and the Ph.D. degree in underwater robotics from The University of Southampton, Southampton, U.K., in 2002 and 2006, respectively. He is Associate Professor at the University of Southampton with a cross appointment with the Institute of Industrial Science, The University of Tokyo. His research interests focus on developing scalable methods for visual and in-situ chemical seafloor observation through improved sensing and autonomy. He is dedicated to fielding real systems in real environments and overcoming bottlenecks in the flow of information from data collection to human insight.

Adrian Bodenmann (M09) received the M.Sc. degree in microengineering from the Ecole Polytechnique Fdrale de Lausanne (EPFL), Lausanne, Switzerland, in 2009. At present he is working at the University of Southampton as a senior research assistant. His research interests are the development of camera systems for high altitude seafloor mapping and algorithms for generating 3D seafloor reconstructions based on photos of the seafloor. He also works on quantifying the certainty in these reconstructions and identifying correlations between identified objects in reconstructions and data from acoustic and chemical sensors.

Ura Tamaki (M91SM02F07) graduated from the Faculty of Engineering, The University of Tokyo, Japan, in 1972 and received the degree of Doctor of Engineering from the same university in 1977. He is at present the Professor emeritus of The University of Tokyo and Director, Distinguished Professor of Center for Socio-Robotic Synthesis, Kyushu Institute of Technology, and Director of Underwater Technology Center of National Maritime Research Institute. He has developed various types of Autonomous Underwater Vehicles (AUVs) and related application technologies including navigation methods, a new sensing method using a chemical sensor, precise seafloor mapping methods, a precise seabed positioning system with a resolution of a few centimeters, a new sensing system of the thickness of cobalt-rich crust, etc. Finally, he exemplified using these technologies that AUVs are practicable and valuable tools for deep-sea exploration.